GENETICS

Gold-DNA nanosunflowers for efficient gene silencing with controllable transformation

Shuaidong Huo[1,2,3]*[†], Ningqiang Gong[1,3]*, Ying Jiang[4], Fei Chen[3,5], Hongbo Guo[1], Yaling Gan[1], Zhisen Wang[6], Andreas Herrmann[2], Xing-Jie Liang[1,3][†]

The development of an efficient delivery system for enhanced and controlled gene interference–based therapeutics is still facing great challenges. Fortunately, the flourishing field of nanotechnology provides more effective strategies for nucleic acid delivery. Here, the triplex-forming oligonucleotide sequence and its complementary strand were used to mediate self-assembly of ultrasmall gold nanoparticles. The obtained sunflower-like nanostructures exhibited strong near-infrared (NIR) absorption and photothermal conversion ability. Upon NIR irradiation, the large-sized nanostructure could disassemble and generate ultrasmall nanoparticles modified with *c-myc* oncogene silencing sequence, which could directly target the cell nucleus. Moreover, the controlled gene silencing effect could be realized by synergistically controlling the preincubation time with the self-assembled nanostructure (in vitro and in vivo) and NIR irradiation time point. This study provides a new approach for constructing more efficient and tailorable nanocarriers for gene interference applications.

INTRODUCTION

Gene therapy showed great potential in the treatment of various diseases, including infertility, HIV, cancer, etc. (*1*). The success of gene therapy, e.g., in cancer treatment, is mainly dependent on the development of an efficient gene delivery vector (*2*). During the delivery process, the gene carrier must cross multiple biological barriers and the cell membrane, as well as escape endosomal entrapment and degradation by nucleases (*3*). Compared with virus-based delivery strategies, nonviral gene delivery approaches face substantial challenges not only regarding the loading and release of DNA/RNA, targeted delivery, and intracellular uptake but also with respect to the issues of biocompatibility and immune response (*4*, *5*).

Currently, the vigorous effort in nanotechnology provides great potential in engineering more stable and efficient vehicles for gene transfer to cancer cells. Owing to their unique physical-chemical properties, numbers of nanomaterials have emerged and been used in gene delivery (*6*–*8*). Among them, gold nanoparticles (Au NPs) with specific size and surface functionalization can overcome obstacles associated with cellular, local, and systemic delivery of gene sequences, which has become one of the most studied gene carrier systems in vitro and in vivo (*3*, *9*). One important approach was introduced by Mirkin and colleagues in 2006 (*10*). They reported a type of spherical nucleic acid, in which Au NPs improve the stability of oligonucleotides and prevent their degradation by nucleases, meanwhile exhibiting more than 99% cellular uptake to reach a high effective concentration. Inspired by their work, our group previously selected ultrasmall (~2 nm) Au NPs to deliver triplex-forming oligonucleotides into a nucleus, directly interfering

with gene transcription process without using any nuclear targeting sequence (*11*). In subsequent work, we demonstrated that variation of particle core size (<10 nm) and surface functionalization could be used synergistically to control the cellular uptake processes (*12*).

However, these strategies still face some shortcomings. On one hand, the net uptake amount of ultrasmall NPs is still low because of cell exocytosis, which resulted in little therapeutic effect (*13*). On the other hand, efficient clearance of the particles from the body represents a critical requirement of safe translation of NPs to clinical practice for disease treatment (*14*). To take advantage of both enhanced nuclear internalization of small-sized NPs and enhanced tumor accumulation/retention of large-sized NPs (*15*), stimuli-responsive drug delivery systems were developed (*16*), which shrink their size by responding to internal tumor microenvironments [e.g., enzymes (*17*), low pH (*18*), etc.] or external stimuli [e.g., ultraviolet (UV) (*19*), near-infrared (NIR) irradiation (*20*), magnetic field (*21*), etc.]. Most representatively, Fukumura and colleagues proposed a multistage NP system composed of a gelatin core with amino–polyethylene glycol quantum dots conjugated to the rim, in which the engineered 100-nm NPs can shrink to 10 nm after they extravasated from leaky regions of the tumor vasculature and being exposed to the overexpressed protease (matrix metalloproteinase-2) in the tumor microenvironment (*17*). Similarly, Tan and colleagues assembled a DNA-based nuclear-uptake nanodrug system carrying a cell-targeted NIR-responsive nanotruck for drug-resistant cancer therapy (*22*). By using this size-photocontrollable nanodrug delivery system, anticancer drugs were efficiently accumulated in the nuclei to effectively kill cancer cells. In a recent publication, Wang and colleagues reported a smart polymeric clustered nanoparticle (iCluster), which exhibits an initial size of ~100 nm (*23*). Once iCluster accumulated at tumor sites, the intrinsic tumor extracellular acidity triggered the discharge of platinum prodrug-conjugated poly(amidoamine) dendrimers (diameter, ~5 nm) to kill cancer cells. Most recently, an effective surface-to-core drug delivery strategy was reported by Kim *et al.* (*24*), in which small Au NPs (~15 nm) with programmable DNA were located in the interconnected channels of silica NPs (~150 nm). This "nanoparticle-loaded nanoparticle" exhibited better accumulation in tumor tissue, and

[1]CAS Center for Excellence in Nanoscience, CAS Key Laboratory for Biomedical Effects of Nanomaterials and Nanosafety, National Center for Nanoscience and Technology, No. 11 First North Road, Zhongguancun, Beijing 100190, P. R. China. [2]DWI–Leibniz Institute for Interactive Materials, Forckenbeckstr. 50, 52056 Aachen, Germany. [3]University of Chinese Academy of Sciences, Beijing 100049, P. R. China. [4]Department of Chemistry, University of Florida, Gainesville, FL 32611, USA. [5]Max Planck Institute for Polymer Research, Ackermannweg 10, 55128 Mainz, Germany. [6]Shijiazhuang Zangnuo Bio Incorporated Corporation, No. 518 Cangsheng Road, Hi-tech District, Shijiazhuang, Hebei Province 050000, P. R. China.
*These authors contributed equally to this work.
†Corresponding author. Email: huosd@nanoctr.cn (S.H.); liangxj@nanoctr.cn (X.-J.L.)

the small Au NPs were subsequently released for deep penetration into the three-dimensional tumor environment. Although those examples are conceptually impressive, there are still plenty of challenges to developing smarter nanosystems simultaneously realizing enhanced tumor retention and cellular uptake, especially realizing controlled therapeutic efficacy. Specifically, it is imperative to establish an efficient delivery system for enhanced and controlled gene interference–based therapeutics.

Inspired by nature's ability to hybridize DNA, DNA-mediated self-assembled gold-DNA nanostructures (~200 nm) were designed and fabricated in this work. As illustrated in Fig. 1, the sunflower-like nanostructures exhibited strong NIR absorption and photothermal conversion ability. Upon NIR irradiation, the large-sized nanostructure could disassemble and liberate ultrasmall Au NPs. The released 2-nm NPs modified with the *c-myc* oncogene silencing sequence improved the NPs nucleus permeability and thus enhanced the transfection efficiency. By synergistically controlling the preincubation time in vitro, circulation time in vivo, and the time point of irradiation, we achieved increased cellular uptake amount,

tunable gene silencing efficacy, and controlled tumor inhibition effect. The transformable nanosunflowers provide an excellent model for the design of nanovehicle, and the system has great potential in biomedical applications.

RESULTS

Self-assembly and characterization of the large-sized nanostructures

We first synthesized 2-nm Au NPs with tiopronin coverage (Au-TIOP NPs) (*25*) and then modified them with thiol-oligonucleotides (SH-POY2T) through a well-established ligand exchange method (*26*). Here, POY2T is a 23-nt (nucleotide) oligonucleotide that can bind with the P2 promoter of the *c-myc* oncogene to form a triplex structure and down-regulate *c-myc* expression of cancer cells (Fig. 1B, step ④) (*27*). Meanwhile, another single-stranded sequence was designed and named as CA to complementarily hybridize with the tail part of POY2T sequence, thus blocking the ability of the POY2T binding with the *c-myc* oncogene. Furthermore, the 2-nm Au-POY2T
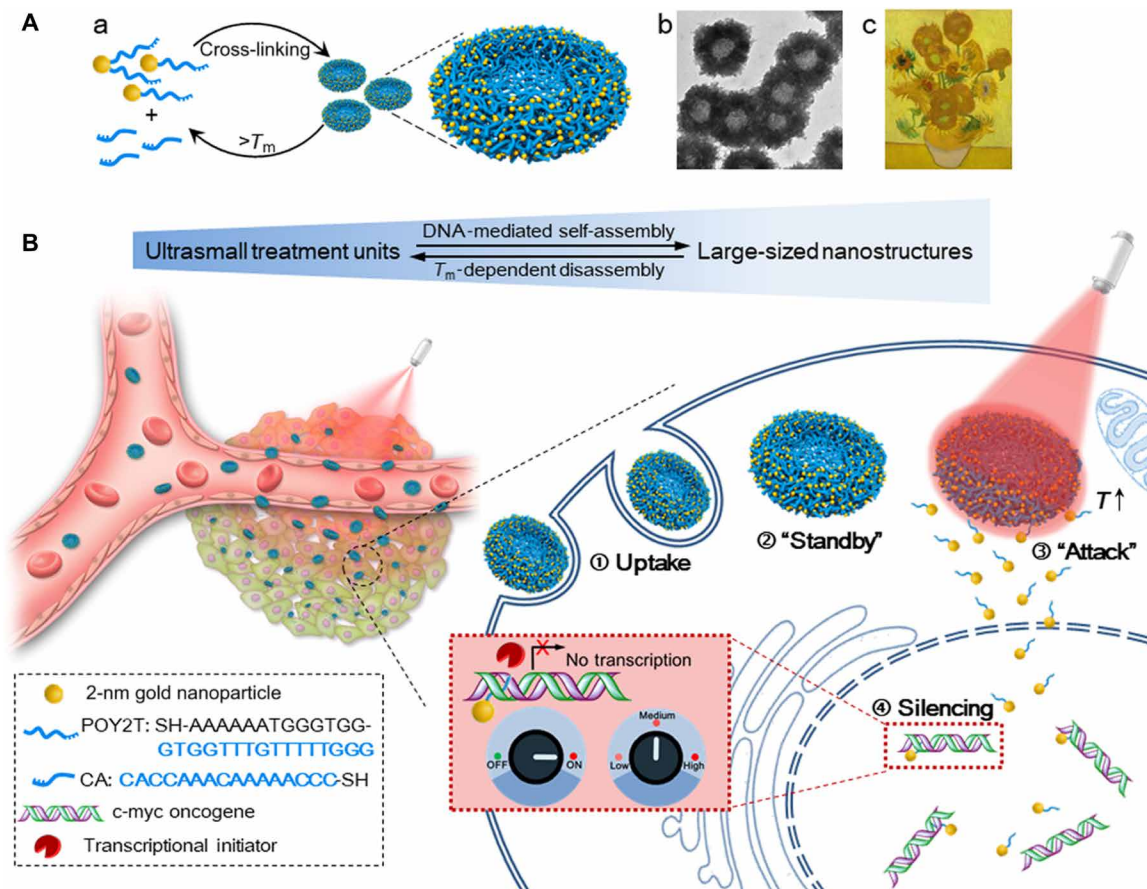
Fig. 1. Scheme of self-assembled gold-DNA nanosunflowers for enhanced cellular uptake amount, tunable gene silencing efficacy, and controlled tumor inhibition effect by NIR irradiation. (**A**) (a) Assembly and disassembly of the large-sized nanostructure (200-nm gold-DNA nanosunflowers) from/to ultrasmall nanoparticles (2-nm Au-POY2T NPs). (b) Representative TEM image of the nanosunflowers. (c) Masterpiece: *Sunflowers* (*Vincent van Gogh, 1889*). (**B**) Left: In vivo tumor retention and penetration of transformable nanosunflowers. Right: Enhanced cellular uptake and controlled oncogene silencing process of the nanosunflowers in vitro. ① Large-sized nanosunflowers were taken up by an MCF-7 cell. ② The nanosunflowers standby in the cell cytoplasm. ③ Upon NIR irradiation, large-sized gold-DNA nanostructures dissociate and release small units (2-nm Au-POY2T NPs) to attack the cell nucleus. ④ The silencing sequence POY2T will bind to the P2 promoter of the *c-myc* oncogene and down-regulate the *c-myc* expression of MCF-7 cells, which can be controlled (ON/OFF) and regulated (Low/Medium/High) by the NIR irradiation.

NPs and CA sequence self-assemble into large-sized sunflower-like structures, as schematically shown in Fig. 1A.

First, the morphology of the self-assembled nanostructures was investigated using electron microscopy techniques. As shown in Fig. 2A, uniform sunflower-shaped nanostructures were identified under the transmission electron microscope (TEM) observation. The size of an individual self-assembled structure was measured to be approximately 200 nm with highly uniform morphology. It was found that nanostructures formed with a thinner center (light in color) and thicker edges (dark in color). It should be pointed out that most of the ultrasmall inorganic NPs were distributed around the outer rim of the nanostructures resulting in the sunflower-like shape (Fig. 1A). At the same time, the bio-TEM with lower voltage (80 kV) captured the same view (Fig. 2B), revealing more details of the polymer constituents representing the DNA moieties of the "sunflower" nanostructures. Moreover, high-resolution TEM images verified the particular edge distribution of small NPs (black dots) at the rim of the sunflower (Fig. 2C). Furthermore, the scanning electron microscope (SEM) confirmed the uniform and unique morphology of the self-assembled nanostructures. As shown in Fig. 2D, the different magnifications of the monodispersed nanostructures indicated the high yield and reliability of the DNA-mediated self-assembly process. Last, enlarged SEM images demonstrated that the center and the edge of the nanostructures

was distinctly different, which was consistent with the TEM observations.

Surface plasmon resonance and photothermal characterization of the self-assembled nanostructures

Previous studies have demonstrated that the surface plasmonic effect of Au NPs could be changed as a result of self-assembly or agglomeration (28). Hence, we next examined the UV-Vis absorption spectra of the ultrasmall Au NPs before and after DNA-mediated self-assembly. As shown in Fig. 3A (blue curve), monodispersed individual 2-nm Au-POY2T NPs (TEM image shown in fig. S1A) did not exhibit significant absorption in the range from 400 to 1000 nm, which is the characteristic spectrum of ultrasmall Au NPs. However, after the DNA-mediated self-assembly process, the obtained nanostructures exhibited a broad and strong absorption in the NIR region (red curve). The surface plasmon resonance absorption band was found from 740 to 810 nm, and the maximum absorption wavelength was centered at 767 nm, which means that the self-assembled nanostructures have significant NIR absorption and could generate heat under NIR irradiation (29). The strong NIR absorbance observed of the self-assembled nanostructure could be attributed to the close interparticle spacing and the nonuniform spatial distribution of the individual ultrasmall particles within the large-sized nanostructure (30).
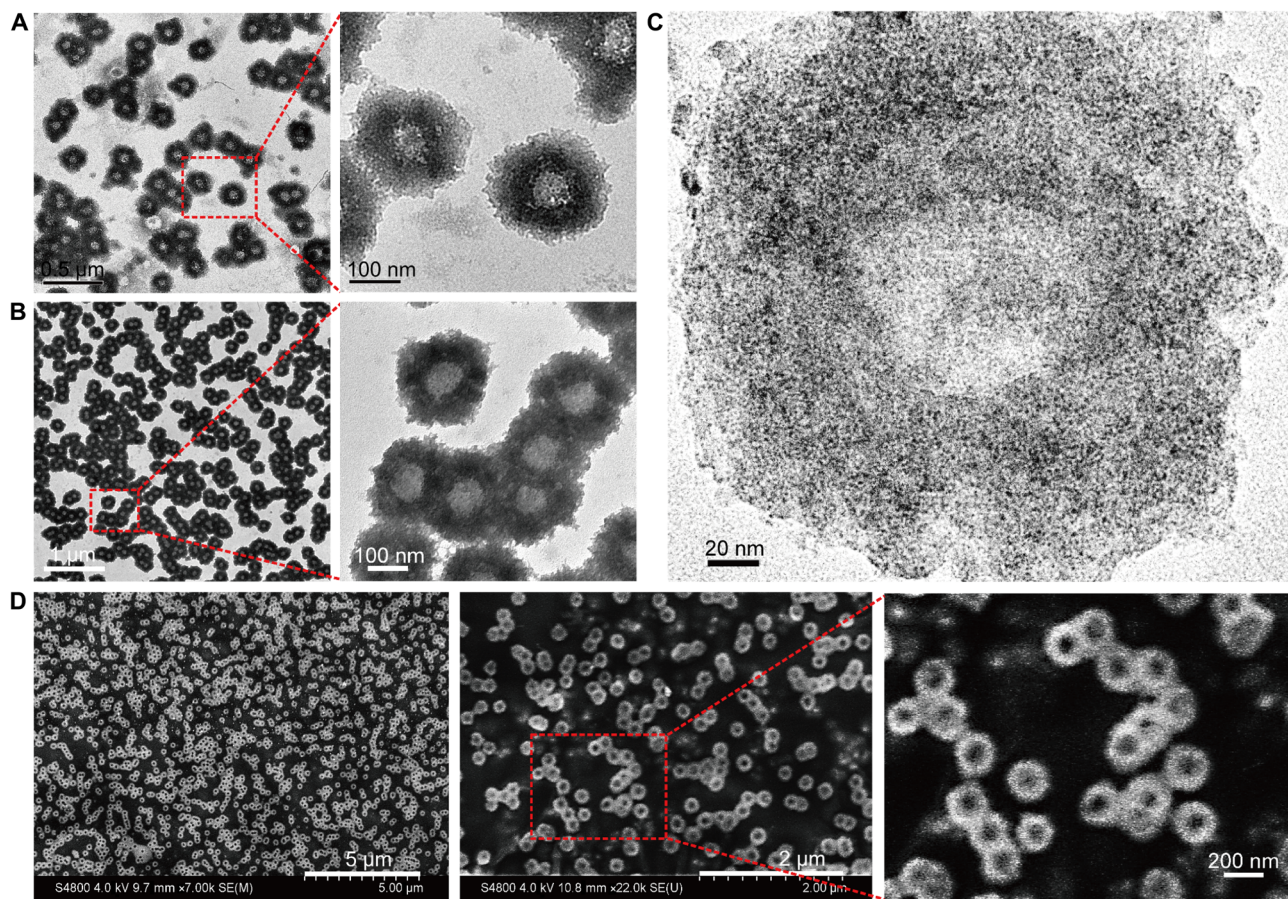
Fig. 2. Morphology characterization of the self-assembled nanostructures (nanosunflowers). (**A**) TEM (200 kV) images of the nanosunflowers with enlarged structural details. (**B**) Bio-TEM (80 kV) images with enlarged polymer structural details. (**C**) High-resolution TEM (200 kV) images showing the distribution of ultrasmall NPs on the self-assembled nanostructure. (**D**) SEM images with enlarged surface topography of the nanosunflowers.
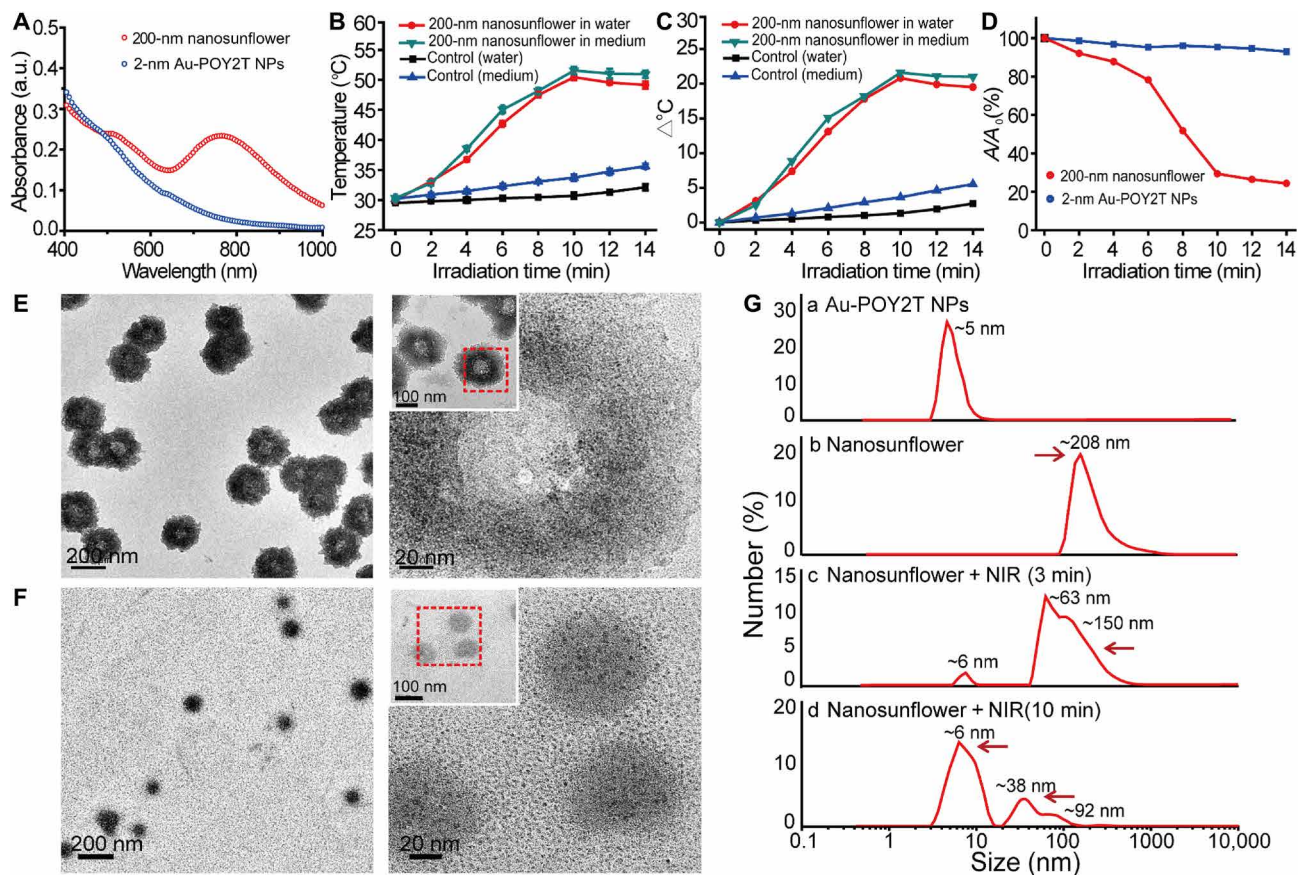
Fig. 3. Photothermal property and disassembly behavior study of the self-assembled nanostructures. (**A**) Visible absorption spectra of 2-nm core-sized NPs and 200-nm self-assembled nanostructures. a.u., absorbance unit. (**B**) Temperature response of self-assembled nanostructures, upon NIR irradiation, dispersed in water and cell culture medium. Mean values ± SD, $n = 3$. (**C**) Temperature rise of self-assembled nanostructures, upon NIR irradiation, dispersed in water and cell culture medium. (**D**) Change of maximum absorbance (767 nm) of 2-nm core-sized NPs and 200-nm self-assembled nanostructures upon NIR irradiation. (**E** and **F**) TEM observation of disassembly behavior of 200-nm self-assembled nanostructures before (top) and after (bottom) NIR irradiation (808 nm, 10 min). (**G**) Hydrodynamic diameter of (a) monodispersed 2-nm Au-POY2T NPs and size change of the 200-nm nanosunflowers before (b) and after (c and d) NIR irradiation for different time periods (3 and 10 min).

We next tested the heat response of the self-assembled nano-structures under NIR irradiation (*31*). According to a formula (*32, 33*), the melting point (T_m) of the complementary DNA sequences (POY2T and CA) selected in this work was calculated to be about ~41°C, which means that half of the duplex structure between POY2T and CA dissociates when the local temperature reaches 41°C. To this end, the photothermal effect of the self-assembled nano-structures was studied. Compared with the control group, as shown in Fig. 3B, the temperature of a solution containing 200-nm nano-structures increased significantly from 30° to ~38°C only after 4-min NIR irradiation (808 nm, 1 W/cm²), and the temperature reached a stable plateau at ~50°C after 10-min irradiation. In con-trast, the temperature rise of the pure water was less than 5°C even after 14-min irradiation (Fig. 3C). Meanwhile, we also measured the heat response of nanostructures dispersed in cell culture medium. A similar photothermal effect was observed. Thus, we chose 10 min as the optimal time for NIR irradiation in the following study.

Disassembly behavior of the self-assembled nanostructures
Triggered by melting dissociation, we hypothesized that the self-assembled nanostructures could shrink and disassemble into in-dividual ultrasmall Au-POY2T NPs (*20, 22*). We found that the

maximum absorption (767 nm) of the self-assembled nanostructures decreased markedly upon 10-min NIR irradiation (Fig. 3D), which indicated the disassembly of the sunflower-like nanostructure. To support this explanation, the NIR-induced disassembly process was followed by TEM observation before and after NIR irradiation. Briefly, 5-μl solution of self-assembled nanostructures was dripped onto a copper mesh and then was irradiated by NIR light for 10 min and dried before TEM observation. Compared with the original morphology of nanostructures shown in Fig. 3E, the self-assembled sunflower-like nanostructures changed significantly after NIR ir-radiation, as shown in Fig. 3F. The 200-nm self-assembled structure was completely destroyed, and the size was largely reduced (<100 nm) as well. Meanwhile, the ultrasmall particles (2-nm Au-POY2T NPs) were restored into the dispersed state and spread throughout on the grid surface (enlarged image shown in fig. S1B). These TEM images directly confirmed the dissociating response of the self-assembled gold-DNA nanostructures upon NIR irradiation, which indicated that the generated heat in proximity of the self-assembled nano-structure could reach the melting temperature of the NP network consisting of the complementary part of POY2T and CA sequence.

In addition to TEM observation, the disassembly process and size transformation of large-sized nanostructures were monitored

by a particle size analyzer. Briefly, the dynamic light scattering size of self-assembled nanostructure was recorded before and after continuous NIR irradiation. As shown in Fig. 3Ga, after a ligand exchange reaction from the original synthesized Au-TIOP NPs (fig. S1C), the hydrodynamic size of 2-nm Au-POY2T NPs was increased to ~5 nm with narrow size distribution. After DNA-mediated self-assembly, the obtained nanostructures exhibited a hydrodynamic size approximately 208 nm (Fig. 3Gb), which was consistent with the electron microscopy characterization above. Upon NIR irradiation for 3 min, the hydrodynamic size of the larger nanostructure decreased and separated into three principal distributions, mainly appearing at ~62, ~150, and ~6 nm (Fig. 3Gc and table S1), which demonstrated that the large-sized nanostructure began to disassemble as triggered by NIR irradiation. Apparently, with the continuous NIR irradiation up to 10 min, most of the ultrasmall particles (>70%, peak approximately ~6 nm) were generated, and the larger particles visibly decreased (Fig. 3Gd). As expected, irradiation with longer time (12.5 or 15 min) more completely disintegrated the large structures (table S1). However, long-time NIR irradiation (>10 min, e.g., 12.5 min) induced significant thermal toxicity to the cells (viability, <70%; fig. S2). Therefore, again, 10 min was confirmed as an optimized NIR irradiation time for the following study. It is reasonable that all the size changes of the self-assembled nanostructure could be attributed to the heat-induced dissociation of the nanostructure under NIR irradiation, which was consistent with the result discussed above.

Together, uniform large-sized nanostructures were self-assembled with sunflower-like morphology, which exhibited significant NIR absorption and photothermal disassembly properties. Triggered by heat-inducing NIR irradiation, the large-sized structures dissociated into smaller parts and generated ultrasmall treatment units (Au-POY2T NPs).

Enhanced cellular uptake of the self-assembled nanostructures

We then tried to apply the NIR irradiation to MCF-7 cells treated with the self-assembled gold-DNA nanostructures and evaluated their cellular uptake level in vitro. Before that, we challenged the stability of the self-assembled nanostructures both in water and 10% fetal bovine serum (FBS)–containing cell culture medium. Compared with dispersing in water, the hydrodynamic diameter of self-assembled nanostructures showed a slight increase (fig. S3), which could be explained by protein adsorption on the surface of nanostructures through electrostatic interaction (34). The formed protein corona thus may protect the nanostructures from degradation by deoxyribonucleases in the cytoplasm (35). The result indicated that the self-assembled nanostructure was kept quite stable when dispersed in cell culture medium even after 24-hour incubation.

Afterward, the cellular internalization of 2-nm Au-POY2T NPs and 200-nm self-assembled nanostructures was studied for different incubation times. The cellular uptake was quantified using inductively coupled plasma mass spectrometry (ICP-MS), and the mass of gold amount was calculated and converted to the number of 2-nm Au NPs using a previously reported method (36, 37). As shown in fig. S4A, the uptake amount of both nanomaterials was increased after each incubation period. Apparently, at the first 3 hours of incubation, the internalization of individual 2-nm Au-POY2T NPs was faster than the larger counterpart. However, after 6-hour incuba-

tion, MCF-7 cells contained more self-assembled nanostructures. The total internalization amount of Au-POY2T NPs contained in larger nanostructures was almost 1.7-fold higher compared to the individual Au-POY2T NP treatment after 24-hour incubation (fig. S4B). The cellular uptake results strongly suggested that different mechanisms could be involved in the cell internalization of both 2-nm Au-POY2T NPs and 200-nm self-assembled nanostructures. Moreover, this could also be explained by the cell exocytosis effect on small-sized NPs (13).

We next compared the effects of various endocytosis inhibitors on the cellular uptake process (fig. S4C) (12). Low temperature and adenosine triphosphate (ATP) depletion can suppress the energy-dependent pathway for NP internalization (38). Cooling cells to 4°C only had limited effects on the uptake of individual 2-nm Au-POY2T NPs but suppressed largely the internalization of the 200-nm self-assembled nanostructures. Similar results were observed by pre-treatment of cells with sodium azide (NaN_3)/2-deoxyglucose (DOG) to deplete ATP, followed by particle treatment at 4° or 37°C. The results indicated that the cellular uptake of large-sized nanostructures was strongly temperature and energy dependent. To understand the cellular uptake pathway in detail, we studied the effects of dynasore, nystatin, methyl-β-cyclodextrin (MβCD), chlorpromazine (CPM), and sucrose, which inhibit dynamin-mediated endocytosis, lipid raft/caveolae–dependent endocytosis, and clathrin-mediated endocytosis, respectively (12). Significantly, all of the inhibitors suppressed the cellular uptake of self-assembled nanostructures, indicating that several endocytosis pathways are involved in the internalization of large-sized nanostructures. Meanwhile, none of the inhibitors showed a notable influence of the uptake on 2-nm Au-POY2T NPs, strongly suggesting that a different pathway, i.e., membrane fusion, was involved in the uptake of 2-nm NPs, which was also consistent with our previous findings (12). Combined with the cellular uptake results and the known cell exocytosis of small-sized NPs (39), we conclude that the self-assembled nanostructures deliver more Au-POY2T NPs into cells than the individual ultrasmall ones for a long time incubation.

Controlled nucleus localization and gene silencing study of the self-assembled nanostructures

Having demonstrated the enhanced cellular uptake of self-assembled nanostructures in vitro, the quantitative distribution of small-sized Au-POY2T NPs in nucleus was thus determined to investigate the controllable "standby" and "attack" (Fig. 1B) strategy after the NIR triggering. As the schematic route shown in Fig. 4A, cell nuclei were extracted for ICP-MS analysis after incubation of individual 2-nm Au-POY2T NPs, self-assembled nanostructures, and self-assembled nanostructures with NIR irradiation after different periods of pre-incubation time (1, 3, 6, and 12 hours). The results indicated that cell preincubation time largely affected the small-sized Au-POY2T NP internalization in the cell nucleus (Fig. 4B). For example, when applying NIR irradiation after 12-hour preincubation, the number of particles in the nucleus (for a total of 24 hours of incubation) was 7.5 times higher than without NIR irradiation and 1.6 times higher than irridation after 1-hour preincubation. Compared with the control group (treated with individual 2-nm Au-POY2T NPs), the number of particles in the nucleus increased to ~170% when treated with self-assembled nanostructures and irradiated after 12-hour preincubation time (fig. S4D). These results demonstrated that the distribution of Au-POY2T NPs in the cell nucleus can be well
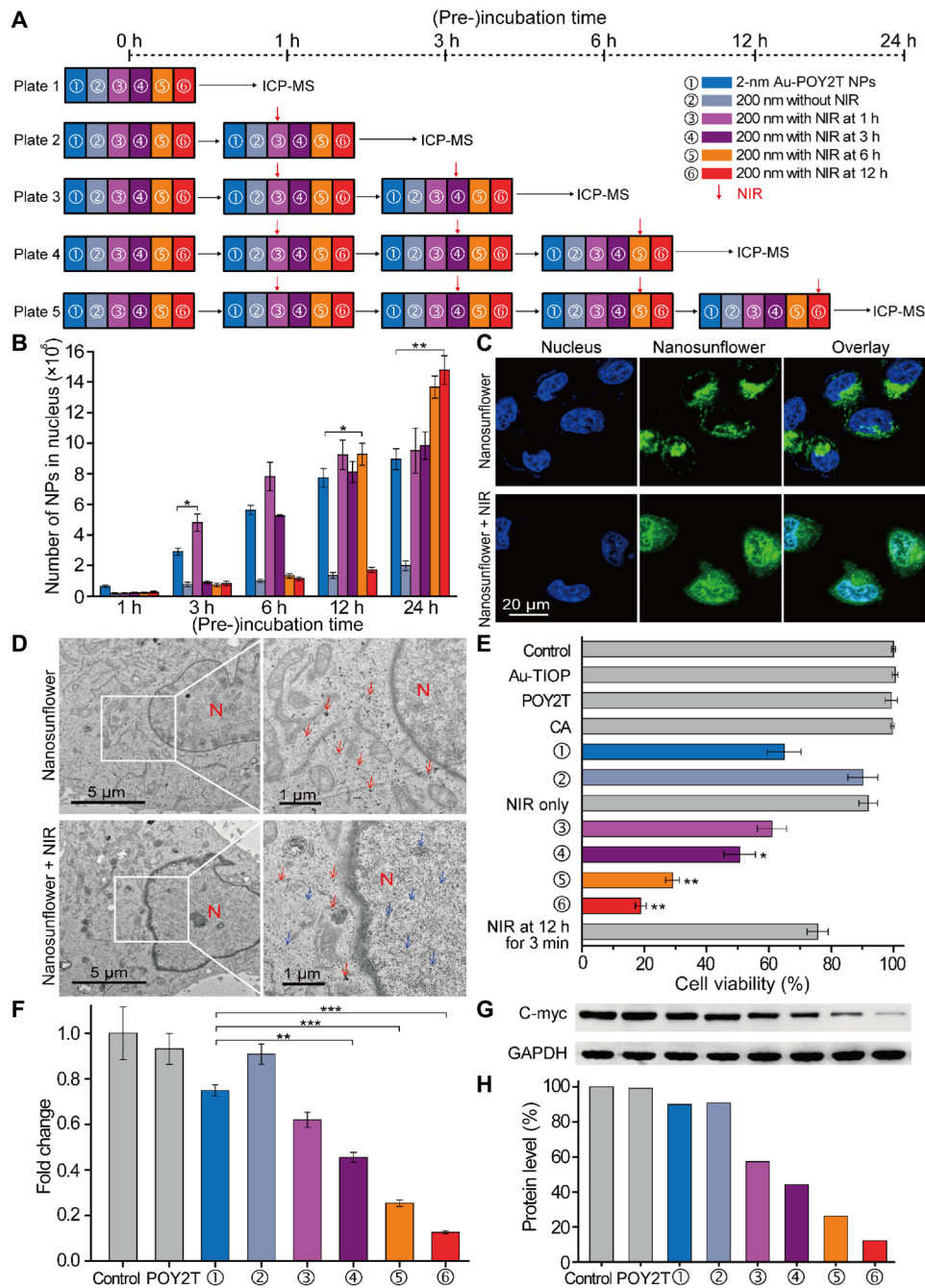
Fig. 4. Controlled nucleus localization and gene silencing study in vitro of the self-assembled nanostructures. (**A**) Schematic of the in vitro cell experimental setup for the controlled NP nucleus localization and gene regulation study. (**B**) Number of 2-nm Au-POY2T NPs localized in the MCF-7 cell nucleus with treatment of ① individual 2-nm Au-POY2T NPs, ② 200-nm nanosunflowers, and 200-nm nanosunflowers with NIR irradiation (10 min) after different preincubation times (③ 1, ④ 3, ⑤ 6, and ⑥ 12 hours). Mean values ± SD, $n = 3$. Statistical differences were determined by two-tailed Student's t test; *$P < 0.05$ and **$P < 0.01$. (**C**) Confocal observation of distribution of fluorescein isothiocyanate–labeled nanosunflowers (green) before (top) and after (bottom) NIR irradiation in MCF-7 cells. Nucleus was labeled by 4′,6-diamidino-2-phenylindole (blue). (**D**) Bio-TEM image of the localization of large-sized nanosunflowers (top, red arrow) in the cytoplasm and distribution of released small NPs (bottom, blue arrow) in cytoplasm and nucleus after NIR irradiation in MCF-7 cells. (**E**) Cytotoxicity evaluation of MCF-7 cells with treatment of 200-nm nanosunflowers after NIR irradiation (after a period of preincubation time: 1, 3, 6, and 12 hours, respectively) compared to control, 2-nm Au-TIOP NPs, POY2T sequence, CA sequence, 2-nm Au-POY2T NPs, 200-nm nanosunflowers without NIR irradiation, and NIR exposure only. All the concentrations of treatments were at or equal to 1 μM in POY2T sequence and were tested after a total of 24 hours of incubation. Mean values ± SD, $n = 3$. Statistical differences were compared with the treatment group of ① individual 2-nm Au-POY2T NPs determined by two-tailed Student's t test; *$P < 0.05$ and **$P < 0.01$. (**F**) C-myc mRNA level determined by real-time PCR after different treatments as described above. Mean values ± SD, $n = 3$. Statistical differences were determined by two-tailed Student's t test; **$P < 0.01$ and ***$P < 0.001$. (**G**) C-myc protein levels determined by Western blot and (**H**) corresponding quantitative histogram after different treatments as described above. GAPDH, glyceraldehyde phosphate dehydrogenase.

controlled by regulating the cell preincubation time and the time point of NIR irradiation.

At the cellular level, with increasing preincubation time, more self-assembled nanostructures were endocytosed and standby in the cytoplasm, which was further observed by a confocal and Bio-TEM study (Fig. 4, C and D) (40). After applying NIR irradiation, the produced heat dissociated the gold-DNA structures and released the small-sized Au-POY2T NPs, which can directly enter the cell nucleus. These results obviously indicated that the large-sized assemblies have much higher selectivity and efficiency to transport these small-sized Au-POY2T NPs into the cell cytoplasm and the nucleus than simple treatment with pristine small Au-POY2T NPs.

Thereafter, the NIR irradiation–controlled therapeutic effect of the nanosunflowers was evaluated by cell viability tests. As shown in Fig. 4E, the anticancer activity (oncogene silencing effect) of the nanosunflowers increased markedly (>80%) when NIR irradiation was applied after 12-hour preincubation time. Compared with the treatment of individual 2-nm Au-POY2T (30%), the self-assembled nanostructure killed more than double the cancer cells. The therapeutic effect can be controlled efficiently and accurately by changing the cell preincubation time and the irradiation time point. It is worth noting that insufficient irradiation time (e.g., 3 min) did not liberate enough small Au-POY2T NPs to achieve significant gene silencing. This behavior can be explained by the photothermal response results (Fig. 3) as discussed above. Moreover, *c-myc* gene expression and protein levels were determined by reverse transcription polymerase chain reaction (PCR) and Western blots, respectively, to confirm the controllable gene regulation process. As shown in Fig. 4F, the pristine POY2T sequence and the self-assembled nanostructures exhibited limited *c-myc* gene silencing ability. Treatment with individual Au-POY2T NPs decreased the *c-myc* mRNA level to about 74.9%. However, NIR irradiation at time points of 1, 3, 6, and 12 hours after the incubation with self-assembled nanostructures displayed 62.0, 45.5, 25.4, and 12.6% of *c-myc* gene suppression, respectively. Separate *c-myc* mRNA level evaluation in cytoplasm and nucleus (fig. S5) also confirmed that the nanosunflowers process better knockdown of *c-myc* in nucleus versus cytoplasm in the presence of NIR irradiation. Further determination of the *c-myc* protein levels in the different treatment groups supported the NIR-controlled protein silencing by the nanosunflowers (Fig. 4, G and H). Together, these results demonstrated a superior ability of the transformable nanostructure in silencing of the *c-myc* oncogene and oncoprotein compared with the free POY2T sequence and individual Au-POY2T NPs. Moreover, the effectiveness of *c-myc* silencing can be precisely controlled by tuning cell preincubation time before applying NIR irradiation.
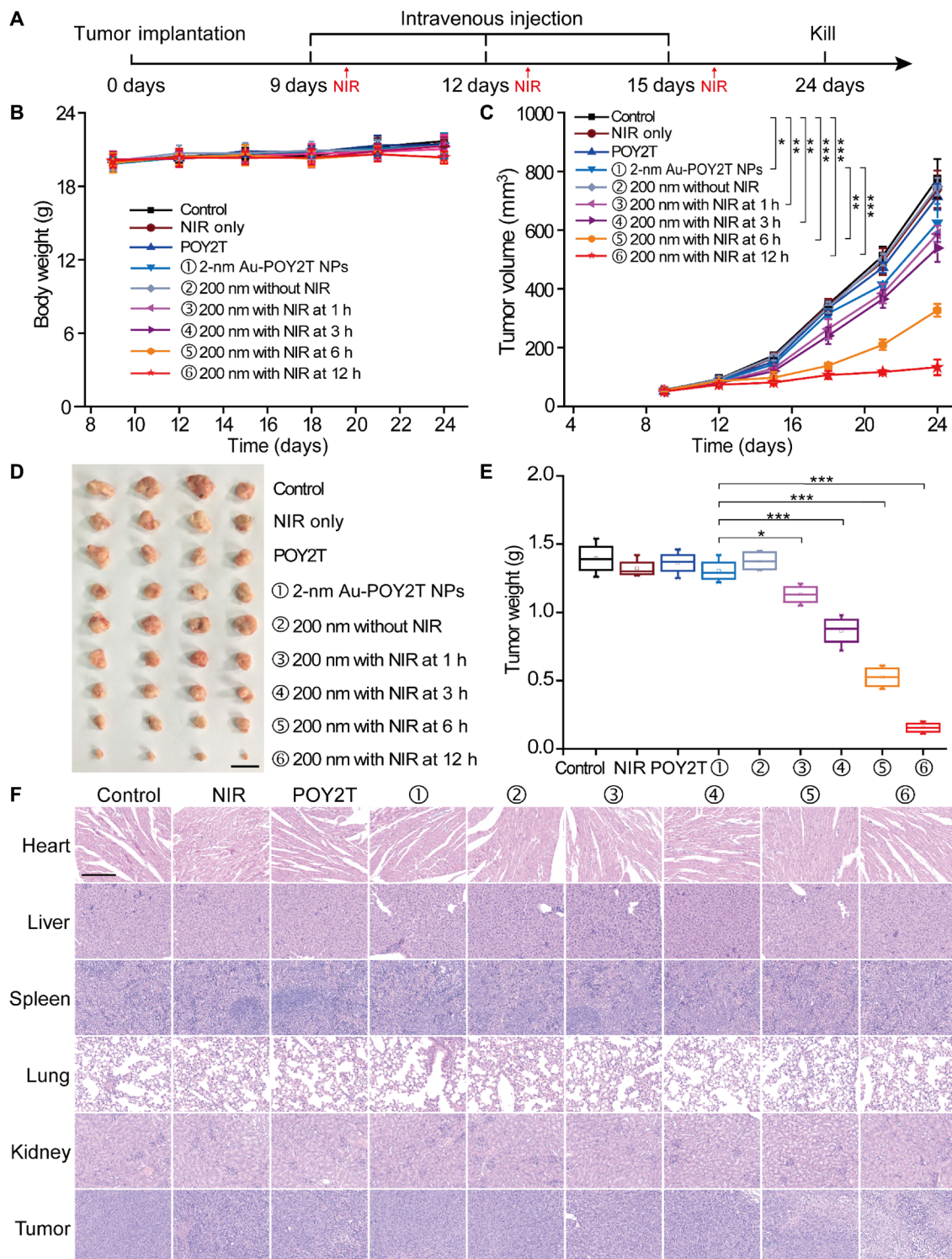
Controlled tumor growth inhibition study of the self-assembled nanostructures

Before testing the controllable antitumor efficiency of nanosunflowers in vivo, we investigated blood compatibility of the assembled nanostructures. As shown in fig. S6A, nanosunflowers with concentrations ranging from 1 nM to 20 µM (at an equivalent POY2T dose) did not show obvious hemolysis of mouse red blood cells. Further blood biochemistry analysis (fig. S6B) also confirmed the good blood compatibility of nanosunflowers obtained in this work. Then, the MCF-7 tumor model was established by using BALB/c nude mice at day 0. After tumor volumes reached about 50 mm³, the animals were randomly divided into nine groups.

Then, the mice were treated with 100 µl of various formulations (equivalent to 10 µM in POY2T) at days 9, 12, and 15 (Fig. 5A). After each intravenous injection, the tumor-bearing mice in groups ③, ④, ⑤, and ⑥ were irradiated with a NIR laser for 10 min (to reach a local temperature above ~41°C) at 1, 3, 6, and 12 hours. During the animal experiment, no obvious body weight altering was observed (Fig. 5B), indicating good biocompatibility of nanosunflowers. As shown in Fig. 5C, mice treated with NIR showed no effect on tumor growth, demonstrating that light irradiation is safe and does not contribute to tumor inhibition. Noteworthy, mice treated with POY2T, Au-POY2T NPs, nanosunflowers, or nanosunflowers with NIR irradiation at 1 or 3 hours showed a slight decrease of tumor volume. Meanwhile, mice treated with nanosunflowers and irradiated at 6 hours after intravenous injection induced significant suppression of tumor growth. The most notable antitumor effect was shown in the nanosunflower-treated group irradiated at 12 hours after intravenous injection, and the tumor volume was about 1/10 compared to the control group, indicating the efficient delivery of gene silencing units into the tumor site. In addition, the NIR-triggered penetration enhancement of nanosunflowers was further demonstrated by an MCF-7 multicellular spheroid model (fig. S7) (17), which well explained the notable antitumor consequence of these nanoagents. After the mice were sacrificed at day 24, all tumors were isolated and weighted (Fig. 5, D and E), together demonstrating that the nanosunflowers showed a NIR-controlled tumor growth inhibition in vivo. The quantified gold amounts inside tumors (fig. S8) also correlate to the tumor uptake of NPs very well with the therapeutic efficacy. In addition, the hematoxylin and eosin (H&E) staining slides and semiquantitative scoring results (Fig. 5F and table S2) showed no histological morphology change of organs, including the heart, liver, spleen, lung, and kidney, after different treatments, indicating that nanosunflowers and NIR therapy have no remarkable side effect on normal tissues. In contrast, there was serious structure damage, a large number of inflammatory cell infiltrations, and a significant cell death in the tumor tissues, especially in groups ⑤ and ⑥, exhibiting the excellent theranostic capability of nanosunflowers.

DISCUSSION

For a long time, the therapeutical effect of nanomedicine has been greatly challenged by complicated tumor microenvironments. As discussed above, it is almost impossible for nanoagents with a fixed size to achieve long time blood circulation, effective accumulation in tumor through the enhanced permeability and retention effect, deep tumor penetration, and efficient cell uptake at the same time. Recently, more and more attention has been paid on this "size relativity" rule by the nanomedicine community. To overcome the multiple biological barriers during the drug delivery, nanodrugs should be rationally designed. In this work, self-assembled sunflower-like nanostructures act as multiparticle carriers, which are loaded with numerous ultrasmall therapeutic units. At the cellular level, the endocytosis pathway of the large-sized nanostructure transports more small NPs inside the cells compared to a membrane fusion process of individual ultrasmall NPs. When applying NIR irradiation as a trigger, self-assembled nanostructures dissociate and disassemble, thereby releasing a large number of small NPs to target the nucleus. In tumor-bearing mice models, large-sized nanosunflowers passively target the tumor site at the first stage. With the NIR triggered

Fig. 5. Controlled tumor growth inhibition study of the self-assembled nanostructures. (**A**) The MCF-7 tumor BALB/c nude mice model was established at day 0. After tumors were ready, the mice were randomly divided into nine groups and treated with 100 μl of various formulations (equivalent to 10 μM in POY2T sequence; group ① with 2-nm Au-POY2T NPs and groups ②, ③, ④, ⑤, and ⑥ with 200-nm nanosunflowers) at days 9, 12, and 15. In groups ③, ④, ⑤, and ⑥, the tumors were irradiated with a NIR laser for 10 min at 1, 3, 6, and 12 hours after each intravenous injection. Saline, NIR only, and POY2T were used as control groups. The (**B**) body weights and (**C**) tumor volumes were measured every 3 days. Scale bar, 1 cm. After the mice were sacrificed at day 24, all tumors were (**D**) isolated and (**E**) weighted, respectively. Mean values ± SD, $n = 4$. Statistical differences were determined by two-tailed Student's t test; $*P < 0.05$, $**P < 0.01$, and $***P < 0.001$. (Photo credit: Ningqiang Gong, National Center for Nanoscience and Technology, China.) (**F**) Hematoxylin and eosin staining images of organs including the heart, liver, spleen, lung, kidney, and tumor after different treatments. Scale bar, 200 μm.

transformation and shrinkage, those particles penetrate into the deeper tumor tissue and were taken up by cells (*15*, *17*, *20*). As a result, the efficient and controllable gene down-regulation was achieved, and the tumor growth was significantly inhibited as well.

The nanosunflower-based gene delivery system could be as follows: (i) A safe and controllable gene delivery tool. Gene silencing can only be activated by NIR irradiation, which occurs only at tumor sites and without side effects to normal tissues. (ii) An effective nuclear delivery vehicle. Genes/drugs can be protected by nano-sunflowers from degradation/inactivation in cytoplasm and be delivered to the nucleus directly permeating the nuclear pore complex by as-released ultrasmall carriers. (iii) A switchable/tunable architecture for selective activation of nanomedicine. By NIR-triggered disassembly, the prodrugs were converted into active moieties switching "on" their properties for disease treatment.

In summary, a DNA-mediated self-assembled nanostructure was designed and fabricated in this work. The uniform sunflower-like nanostructure exhibited strong NIR absorption and showed a sensitive photothermal response. By synergistically controlling both the preincubation time in vitro (or circulation time in vivo) and the NIR irradiation time point, the transfection efficiency can be gradually controlled down to a minimum level. The obtained results of this study provide a blueprint for constructing transformable gene interference carriers with intricate functionality to adjust expression levels of genes with external control.

MATERIALS AND METHODS
Preparation of 2-nm Au-POY2T NPs
First, 2-nm Au-TIOP NPs were synthesized using a previously reported method (*25*). Typically, 6 ml of methanol, 1 ml of acetic acid, and 5 ml of 1% $HAuCl_4$ were mixed and kept stirring for 5 min, and 64 mg of tiopronin powder was added under vigorous stirring. After the solution changed color to nearly colorless, $NaBH_4$ solution (100 mg in 500 μl of ice-cold water) was added into the above mixture under vigorous stirring. The reaction was terminated after 3 hours, and the resulting mixture was dialyzed (dialysis membrane, Solarbio; molecular weight cutoff, 8000 to 14,000 Da) against Milli-Q water for 72 hours, which was changed every 8 hours. Two-nanometer Au-POY2T NPs were obtained by replacing the tiopronin on the surface of Au-TIOP NPs with thiol-modified oligonucleotides (SH-POY2T: SH-C6-AAAAAATGGGT GGGTGGTTTGTTTTTGGG) through a ligand exchange method (*26*). SH-POY2T sequence was first treated by 5 mM Tris-(2-carboxyethyl)-phosphine (TCEP) for 30 min in phosphate-buffered saline (PBS) buffer. Then, 2-nm Au-TIOP NPs were added and kept stirring at room temperature for 24 hours. The exchange efficiency was determined by gel electrophoresis, and the intensity of the band indicates that ~50% POY2T were conjugated to the 2-nm Au NPs.

Self-assembly of the larger-sized nanostructures
Thiol-modified CA sequence (10 μM; SH-C6-CCCAAAAACAAAC-CAC) was first treated by 5 mM TCEP for 30 min in PBS buffer, followed by addition of 3 × PBS, 5 mM $MgCl_2$, 10 mM $NaHPO_4$, and kept stirring for 3 min. Then, the freshly prepared 2-nm Au-POY2T NPs was added to the above solution, was heated to 60°C, and was reacted for 10 min. Last, the reaction was kept stirring at 35°C for another 2 hours, then cooled down to room temperature. Before further use, the obtained solution was washed twice by PBS at

5000 rpm for 5 min to remove the free particles, unbounded sequences, and excess molecules. The gold concentration of assembled nanostructures was determined by the ICP-MS method, calculated and converted to the 2-nm Au NPs.

Heat response study of the self-assembled nanostructures under the NIR irradiation
Briefly, aqueous solution and cell culture medium containing self-assembled nanostructures (equivalent to 20 μM in POY2T sequence) were irradiated by using an 808-nm NIR laser at 1 W/cm² for 14 min. The temperature of solutions was measured by a digital thermometer and recorded at different time points. Water and cell culture medium were used as blank controls, and each measurement was done in triplicate. The theoretical melting temperature (T_m) of DNA was calculated by the formula: $T_m = (wA + xT) \times 2 + (yG + zC) \times 4$, where w, x, y, and z are the number of the bases A, T, G, and C in the sequence, respectively (*32*).

Cell culture
MCF-7 cells (human breast cancer cell line) were purchased from the American Type Culture Collection (Manassas, VA) and maintained in low-glucose Dulbecco's modified Eagle's medium with 10% FBS and 1% antibiotic [penicillin (100 U/ml) and streptomycin (100 μg/ml)]. The cells were cultured in a water-jacketed CO_2 incubator (Forma Series II 3110, Thermo Fisher Scientific Inc., USA) providing a humidified atmosphere with 5% CO_2 at 37°C.

Cell uptake study
MCF-7 cells were seeded in a 48-well plate at a density of ~ 2×10^4 cells per well 24 hours a day before the experiment. At the day of incubation, cells were washed three times with PBS, and as-synthesized 2-nm Au-POY2T NPs and self-assembled nanoflowers (calculated as the number of Au-POY2T NPs from the gold element amount) were added at a concentration of 100 nM and incubated at different times (1, 3, 6, 12, and 24 hours) at 37°C. After each incubation, the cells were washed three times with PBS buffer. Cell lysis buffer (250 μl per well) was used to lyse the cells, and the culture plate was kept at room temperature on a vibrator for 30 min. In addition, a freeze/thaw cycle was adopted to further facilitate the cell lysis process before the ICP sample preparation step.

Cell uptake inhibition study
MCF-7 cells were seeded in a 48-well plate at a density of ~2×10^4 cells per well 24 hours in advance. At the day of experiment, cells were washed three times with PBS and preincubated with the following endocytic inhibitors in complete medium for 2 hours at 37°C: MβCD (10 mM), nystatin (180 nM), sodium azide (NaN₃, 10 mM) + DOG (50 mM), dynasore (80 μM), CPM hydrochloride (20 nM), and sucrose (450 mM). For temperature- and energy-dependent pathway study, cells were pretreated with 10 mM NaN₃ and 50 mM DOG at 4°C for 2 hours. The concentrations of the inhibitors were used according to previous reports (*12*). After 2 hours, Au-POY2T NPs and self-assembled nanoflowers were added at a concentration of 100 nM of Au-POY2T NPs and incubated for another 22 hours at 37°C in the presence of the inhibitors. Untreated cells were used as a negative control, and cells treated with only NPs in the absence of inhibitors were used as a positive control. After incubation, cells were washed three times with PBS buffer, and cell lysis buffer (250 μl per well) was used to lyse the cell. The

cell culture plate was kept at room temperature on a vibrator for 30 min. In addition, a freeze/thaw cycle was adopted to further facilitate the cell lysis process before the ICP sample preparation step.

Cell nucleus localization study

The experimental setup of the cell nucleus localization study was schemed as shown in Fig. 4A. For each 96-well plate, a number of ~10^4 MCF-7 cells were seeded 24 hours in advance. Afterward, 100 nM 2-nm Au-TIOP NPs or self-assembled nanoflowers (equal concentration calculated as 100 nM of Au-POY2T NPs from the gold element amount) were suspended in fresh media and added to the wells. After each preincubation point, the cells were irradiated by a NIR laser for 10 min and ready for ICP-MS analysis after further incubation. Before ICP-MS sample preparation, nuclear extraction of the cells was processed. Briefly, the cells were washed with PBS, trypsinized, and centrifuged for 3 min at 179g. The treated cells were resuspended in 1 ml of PBS and were handled for cell nucleus extraction using a nuclear extraction kit (SN000, Solarbio, Shanghai, China). Briefly, the sample was ground in lysis buffer for 3 min, centrifuged at 700g for 5 min, resuspended in lysis buffer, precipitated in medium buffer, and stored in a store buffer. All the procedures were carried out at 4°C quickly to keep nucleus integrity. The extracted nuclei were analyzed by ICP-MS after a nitrolysis procedure.

Cell viability study with NIR laser irradiation

MCF-7 cells (10^4 cells per well) were seeded in 96-well plates for 24 hours in advance. Afterward, 2-nm Au-POY2T NPs, self-assembled nanoflowers, and other control groups (POY2T sequence, CA sequence, and 2-nm Au-TIOP NPs) were suspended in fresh media and added to the wells. All the treated concentrations were at or equal to 1 μM in POY2T. For self-assembled nanostructure-treated groups, the cells were irradiated by an 808-nm NIR laser at 1 W/cm^2 for 3 or 10 min after each preincubation (1, 3, 6, and 12 hours). After each irradiation, the cells were continued for incubation until 24 hours. Last, the cell viability was determined by an MTT (3-(4,5-dimethylthiazol-2-yl)-2,5-diphenyltetrazolium bromide) assay. Briefly, the medium was replaced with 100 μl of MTT (0.5 mg/ml), and after a 3-hour incubation, the MTT solution was replaced with 150 μl of dimethyl sulfoxide solution. The absorbance at 570 nm of each well was measured by a plate reader. Untreated cells in the medium were used as a control. All SDs were calculated from three replicates.

Tumor inhibition study

BALB/c nude mice (6 weeks, female) were obtained from Beijing Charles River Laboratory Animal Technology Co. Ltd. (Beijing, China) and raised in a specific pathogen–free grade laboratory. All animal experiments were performed in accordance with the *Guide for the Care and Use of Laboratory Animals* proposed by the National Institutes of Health (NIH). All animal experiments were conducted with the approval of the Institutional Animal Care and Use Committee, Institute of Process Engineering, Chinese Academy of Sciences. Briefly, the MCF-7 tumor model was established by subcutaneous injection of 10^6 MCF-7 cells into the right flank of BALB/c nude mice (about 20 g) at day 0. After tumor volumes reached about 50 mm^3, the animals were randomly divided into nine groups (four mice per group). Then, the mice were treated with 100 μl of various formulations (equivalent to 10 μM in POY2T sequence) at days 9, 12, and 15 by intravenous injection. In groups ③, ④, ⑤, and ⑥

(as labeled in Fig. 5), the tumors were irradiated with an 808-nm NIR laser (1 W/cm^2) for 10 min (to reach the local temperature above 41°C) at 1, 3, 6, and 12 hours after each intravenous injection. In day 24, the mice were sacrificed, and all tumors were isolated and weighted.

Statistical analysis

All data are expressed as means ± SD. Statistical differences were determined by two-tailed Student's t test; *P < 0.05, **P < 0.01, and ***P < 0.001. The density of Western blot bands was quantified using ImageJ software (NIH Image).

SUPPLEMENTARY MATERIALS

Supplementary material for this article is available at http://advances.sciencemag.org/cgi/content/full/5/10/eaaw6264/DC1

Fig. S1. Characterization of the as-synthesized NPs.
Fig. S2. Cytotoxicity evaluation of MCF-7 cells with NIR irradiation at different times.
Fig. S3. Stability test of self-assembled nanostructures.
Fig. S4. Cellular uptake and intracellular distribution of NPs.
Fig. S5. *C-myc* mRNA level determined in cytoplasm and nucleus separately by real-time PCR.
Fig. S6. Safety evaluation of the nanosunflower structure.
Fig. S7. Penetration behavior study of fluorescein isothiocyanate–labeled nanosunflowers in multicellular spheroid model.
Fig. S8. Quantitative biodistribution of average Au content in tissues including the heart, liver, spleen, lung, kidney, and tumor after different treatments.
Table S1. Hydrodynamic size distribution of Au-POY2T NPs and nanosunflowers before and after NIR irradiation for 3, 10, 12.5, or 15 min, respectively.
Table S2. Histopathological scoring results of the H&E staining images.

REFERENCES AND NOTES

1. A. El-Aneed, An overview of current delivery systems in cancer gene therapy. *J. Control. Release* **94**, 1–14 (2004).
2. S.-D. Li, S. Chono, L. Huang, Efficient oncogene silencing and metastasis inhibition via systemic delivery of siRNA. *Mol. Ther.* **16**, 942–946 (2008).
3. Y. Jiang, S. D. Huo, J. Hardie, X.-J. Liang, V. M. Rotello, Progress and perspective of inorganic nanoparticle-based siRNA delivery systems. *Expert Opin. Drug Deliv.* **13**, 547–559 (2016).
4. R. Waehler, S. J. Russell, D. T. Curiel, Engineering targeted viral vectors for gene therapy. *Nat. Rev. Genet.* **8**, 573–587 (2007).
5. J. Dobson, Gene therapy progress and prospects: Magnetic nanoparticle-based gene delivery. *Gene Ther.* **13**, 283–287 (2006).
6. E. Wagner, Polymers for siRNA delivery: Inspired by viruses to be targeted, dynamic, and precise. *Acc. Chem. Res.* **45**, 1005–1013 (2012).
7. M. Wang, K. Alberti, A. Varone, D. Pouli, I. Georgakoudi, Q. Xu, Enhanced intracellular siRNA delivery using bioreducible lipid-like nanoparticles. *Adv. Healthc. Mater.* **3**, 1398–1403 (2014).
8. J. Conde, A. Ambrosone, Y. Hernandez, F. Tian, M. McCully, C. C. Berry, P. V. Baptista, C. Tortiglione, J. M. de la Fuente, 15 years on siRNA delivery: Beyond the state-of-the-art on inorganic nanoparticles for RNAi therapeutics. *Nano Today* **10**, 421–450 (2015).
9. Y. Ding, Z. Jiang, K. Saha, C. S. Kim, R. F. Landis, V. M. Rotello, Gold nanoparticles for nucleic acid delivery. *Mol. Ther.* **22**, 1075–1083 (2014).
10. N. L. Rosi, D. A. Giljohann, C. S. Thaxton, A. K. R. Lyttom-Jean, M. S. Han, C. A. Mirkin, Oligonucleotide-modified gold nanoparticles for intracellular gene regulation. *Science* **312**, 1027–1030 (2006).
11. S. Huo, S. Jin, X. Ma, X. Xue, K. Yang, A. Kumar, P. C. Wang, J. Zhang, Z. Hu, X.-J. Liang, Ultrasmall gold nanoparticles as carriers for nucleus-based gene therapy due to size-dependent nuclear entry. *ACS Nano* **8**, 5852–5862 (2014).
12. Y. Jiang, S. Hou, T. Mizuhara, R. Das, Y.-W. Lee, S. Hou, D. F. Moyano, B. Duncan, X.-J. Liang, V. M. Rotello, The interplay of size and surface functionality on the cellular uptake of sub-10 nm gold nanoparticles. *ACS Nano* **9**, 9986–9993 (2015).
13. T. M. Sun, Y. S. Zhang, B. Pang, D. C. Hyun, M. Yang, Y. Xia, Engineered nanoparticles for drug delivery in cancer therapy. *Angew. Chem. Int. Edit.* **53**, 12320–12364 (2014).
14. C. Zhou, M. Long, Y. Qin, X. Sun, J. Zheng, Luminescent gold nanoparticles with efficient renal clearance. *Angew. Chem. Int. Edit.* **50**, 3168–3172 (2011).
15. S. Huo, H. Ma, K. Huang, J. Liu, S. Jin, J. Zhang, S. He, X.-J. Liang, Superior penetration and retention behavior of 50 nm gold nanoparticles in tumors. *Cancer Res.* **73**, 319–330 (2013).
16. S. Wang, P. Huang, X. Chen, Hierarchical targeting strategy for enhanced tumor tissue accumulation/retention and cellular internalization. *Adv. Mater.* **28**, 7340–7364 (2016).

17. C. Wong, T. Stylianopoulos, J. Cui, J. Martin, V. P. Chauhan, W. Jiang, Z. Popović, R. K. Jain, M. G. Bawendi, D. Fukumura, Multistage nanoparticle delivery system for deep penetration into tumor tissue. *Proc. Natl. Acad. Sci. U.S.A.* **108**, 2426–2431 (2011).

18. X. Xu, J. Wu, Y. Liu, M. Yu, L. Zhao, X. Zhu, S. Bhasin, Q. Li, E. Ha, J. Shi, O. C. Farokhzad, Ultra-pH-responsive and tumor-penetrating nanoplatform for targeted siRNA delivery with robust anti-cancer efficacy. *Angew. Chem. Int. Edit.* **55**, 7091–7094 (2016).

19. R. Tong, H. H. Chiang, D. S. Kohane, Photoswitchable nanoparticles for in vivo cancer chemotherapy. *Proc. Natl. Acad. Sci. U.S.A.* **110**, 19048–19053 (2013).

20. Z. Xiao, C. Ji, J. Shi, E. M. Pridgen, J. Frieder, J. Wu, O. C. Farokhzad, DNA self-assembly of targeted near-infrared-responsive gold nanoparticles for cancer thermo-chemotherapy. *Angew. Chem. Int. Edit.* **51**, 11853–11857 (2012).

21. E. Ruiz-Hernández, A. Baeza, M. Vallet-Regí, Smart drug delivery through DNA/magnetic nanoparticle gates. *ACS Nano* **5**, 1259–1266 (2011).

22. L. Qiu, T. Chen, I. Öçsoy, E. Yasun, C. Wu, G. Zhu, M. You, D. Han, J. Jiang, R. Yu, W. Tan, A Cell-Targeted, Size-photocontrollable, nuclear-uptake nanodrug delivery system for drug-resistant cancer therapy. *Nano Lett.* **15**, 457–463 (2015).

23. H.-J. Li, J.-Z. Du, X.-J. Du, C.-F. Xu, C.-Y. Sun, H.-X. Wang, Z.-T. Cao, X.-Z. Yang, Y.-H. Zhu, S. Nie, J. Wang, Stimuli-responsive clustered nanoparticles for improved tumor penetration and therapeutic efficacy. *Proc. Natl. Acad. Sci. U.S.A.* **113**, 4164–4169 (2016).

24. J. Kim, C. Jo, W.-. G. Lim, S. Jung, Y. M. Lee, J. Lim, H. Lee, J. Lee, W. J. Kim, Programmed nanoparticle-loaded nanoparticles for deep-penetrating 3D cancer therapy. *Adv. Mater.* **30**, e1707557 (2018).

25. K. Huang, H. Ma, J. Liu, S. Huo, A. Kumar, T. Wei, X. Zhang, S. Jin, Y. Gan, P. C. Wang, S. He, X. Zhang, X.-J. Liang, Size-dependent localization and penetration of ultrasmall gold nanoparticles in cancer cells, multicellular spheroids, and tumors in vivo. *ACS Nano* **6**, 4483–4493 (2012).

26. G. H. Woehrle, L. O. Brown, J. E. Hutchison, Thiol-functionalized, 1.5-nm gold nanoparticles through ligand exchange reactions: Scope and mechanism of ligand exchange. *J. Am. Chem. Soc.* **127**, 2172–2183 (2005).

27. E. M. McGuffie, D. Pacheco, G. M. R. Carbone, C. V. Catapano, Antigene and antiproliferative effects of a *c-myc*-targeting phosphorothioate triple helix-forming oligonucleotide in human leukemia cells. *Cancer Res.* **60**, 3790–3799 (2000).

28. J. Liu, Y. Lu, Preparation of aptamer-linked gold nanoparticle purple aggregates for colorimetric sensing of analytes. *Nat. Protoc.* **1**, 246–252 (2006).

29. X. Huang, S. Neretina, M. A. El-Sayed, Gold nanorods: From synthesis and properties to biological and biomedical applications. *Adv. Mater.* **21**, 4880–4910 (2009).

30. J. M. Tam, J. O. Tam, A. Murthy, D. R. Ingram, L. L. Ma, K. Travis, K. P. Johnston, K. V. Sokolov, Controlled assembly of biodegradable plasmonic nanoclusters for near-infrared imaging and therapeutic applications. *ACS Nano* **4**, 2178–2184 (2010).

31. Z. Li, R. Jin, C. A. Mirkin, R. L. Letsinger, Multiple thiol-anchor capped DNA-gold nanoparticle conjugates. *Nucleic Acids Res.* **30**, 1558–1562 (2002).

32. R. Owczarzy, P. M. Vallone, F. J. Gallo, T. M. Paner, M. J. Lane, A. S. Benight, Predicting sequence-dependent melting stability of short duplex DNA oligomers. *Biopolymers* **44**, 217–239 (1997).

33. K. J. Breslauer, R. Frank, H. Blöcker, L. A. Marky, Predicting DNA duplex stability from the base sequence. *Proc. Natl. Acad. Sci. U.S.A.* **83**, 3746–3750 (1986).

34. A. E. Nel, L. Mädler, D. Velegol, T. Xia, E. M. V. Hoek, P. Somasundaran, F. Klaessig, V. Castranova, M. Thompson, Understanding biophysicochemical interactions at the nano–bio interface. *Nat. Mater.* **8**, 543–557 (2009).

35. C. H. Kapadia, J. R. Melamed, E. S. Day, Spherical nucleic acid nanoparticles: Therapeutic potential. *BioDrugs* **32**, 297–309 (2018).

36. S. Huo, S. Chen, N. Gong, J. Liu, X. Li, Y. Zhao, X.-J. Liang, Ultrasmall gold nanoparticles behavior in vivo modulated by surface polyethylene glycol (PEG) grafting. *Bioconjug. Chem.* **28**, 239–243 (2017).

37. B. D. Chithrani, A. A. Ghazani, W. C. W. Chan, Determining the size and shape dependence of gold nanoparticle uptake into mammalian cells. *Nano Lett.* **6**, 662–668 (2006).

38. L. M. Wang, Y. Liu, W. Li, X. Jiang, Y. Ji, X. Wu, L. Xu, Y. Qiu, K. Zhao, T. Wei, Y. Li, Y. Zhao, C. Chen, Selective targeting of gold nanorods at the mitochondria of cancer cells: Implications for cancer therapy. *Nano Lett.* **11**, 772–780 (2011).

39. N. Oh, J.-H. Park, Endocytosis and exocytosis of nanoparticles in mammalian cells. *Int. J. Nanomedicine* **9**, 51–63 (2014).

40. J. Gilleron, W. Querbes, A. Zeigerer, A. Borodovsky, G. Marsico, U. Schubert, K. Manygoats, S. Seifert, C. Andree, M. Stöter, H. Epstein-Barash, L. Zhang, V. Koteliansky, K. Fitzgerald, E. Fava, M. Bickle, Y. Kalaidzidis, A. Akinc, M. Maier, M. Zerial, Image-based analysis of lipid nanoparticle-mediated siRNA delivery, intracellular trafficking and endosomal escape. *Nat. Biotechnol.* **31**, 638–646 (2013).

Science Advances

Gold-DNA nanosunflowers for efficient gene silencing with controllable transformation

Shuaidong Huo, Ningqiang Gong, Ying Jiang, Fei Chen, Hongbo Guo, Yaling Gan, Zhisen Wang, Andreas Herrmann and Xing-Jie Liang

ARTICLE TOOLS	http://advances.sciencemag.org/content/5/10/eaaw6264
SUPPLEMENTARY MATERIALS	http://advances.sciencemag.org/content/suppl/2019/09/30/5.10.eaaw6264.DC1
REFERENCES	This article cites 40 articles, 7 of which you can access for free http://advances.sciencemag.org/content/5/10/eaaw6264#BIBL
PERMISSIONS	http://www.sciencemag.org/help/reprints-and-permissions